Nano Research

Open Access

Research Article

Unique nanowire assemblies enables superior anti-interference capability for accurate structural failure prediction and soft robotics

Xin-Lin Li[1,§], Cheng Chen[1,§], Zhong-Yuan Yang[2,§], Xiang-Sen Meng[2], Yin-Bo Zhu[3], Xue-Fei Feng[1], Yu-Cheng Gao[2], Wen-Ze Wang[1], and Jian-Wei Liu[1] ✉

[1] *Key Laboratory of Precision and Intelligent Chemistry, Department of Chemistry, University of Science and Technology of China, Hefei 230026, China*

[2] *Division of Nanomaterials & Chemistry, Hefei National Research Center for Physical Sciences at the Microscale, Institute of Energy, Hefei Comprehensive National Science Center, Department of Chemistry, Institute of Biomimetic Materials & Chemistry, Anhui Engineering Laboratory of Biomimetic Materials, University of Science and Technology of China, Hefei 230026, China*

[3] *CAS Key Laboratory of Mechanical Behavior and Design of Materials, Department of Modern Mechanics, CAS Center for Excellence in Complex System Mechanics, University of Science and Technology of China, Hefei 230027, China*

[§] *Xin-Lin Li, Cheng Chen, and Zhong-Yuan Yang contributed equally to this work.*

Cite this article: *Nano Research*, **2025**, *18*, 94906990. https://doi.org/10.26599/NR.2025.94906990

ABSTRACT: Electronic skin (e-skin), capable of perceiving various external stimuli, has emerged as a ubiquitous technology in the field of flexible electronics, finding diverse applications in healthcare systems, prosthetics, and soft robotics. Particularly, anisotropic e-skins have garnered extensive research attention due to their unique directional properties. Nevertheless, the continuous interference from diverse stimuli and intricate environments, along with low sensitivity, have hindered the further widespread application of anisotropic e-skin. Here, we present a transparent e-skin exhibiting remarkable anisotropic strain sensing performance, along with exceptional resilience against interference from other stimuli and harsh environments. Benefiting from the synergistic coexistence of aligned silver nanowires wrinkles and cracks, the e-skin achieves outstanding anisotropy showcasing maximum strain gauge factors (GFs) difference of 2825 and 0.69 along two perpendicular directions, exceeding a difference of more than 4000 times. Furthermore, the e-skin displays superior anti-interference capability, evidenced by a resistance change of less than 6% when subjected to high pressure (663 kPa), torsion (540°), or bending (180°), and exhibits negligible performance degradation even after exposure to harsh environments. Finally, our e-skin is successfully applied to undisturbed predicting crack propagation and precise control of dual-mode soft robots, highlighting its immense potential in structural damage warning and intelligent robotics.

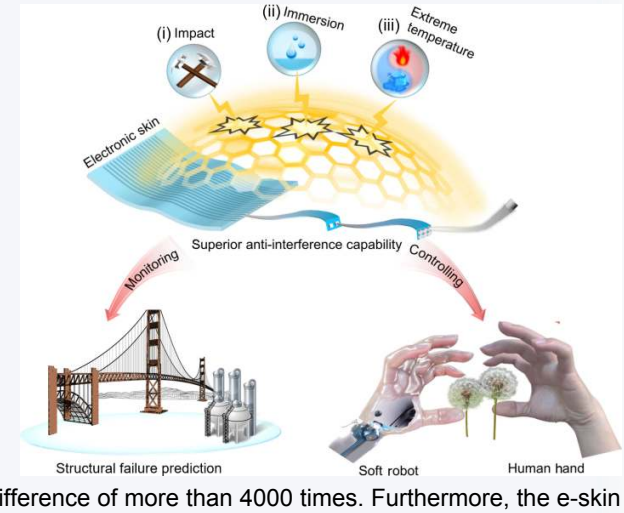

KEYWORDS: nanowire assembly, heterogeneous electronic skin, anti-interference capability, crack prediction, soft robot

1 Introduction

With the rapid evolution of wearable electronics, electronic skin (e-skin) has gained extensive utilization in health monitoring [1–4], biomedical engineering [5–7], virtual reality (VR) [8, 9], human-machine interaction [10–15], and various other applications. In recent years, an increasing number of e-skins with exceptional sensitivity [16, 17], a super extensive response range [18], excellent stability [19], and even self-healing ability [20] have been reported to satisfy growing demand in practical applications. Normally, the majority of electronic skins are capable of responding to a wide range of external stimuli, including strain, pressure, bending, temperature [21–24]. Among these developments, anisotropic e-skin has garnered significant attention due to its unique ability to selectively respond to various directions, simplifying wirings and integrations for omnidirectional detection. However, anisotropic e-skin is usually exposed to various interferences besides stretching in

Received: April 19, 2024; **Revised:** June 3, 2024
Accepted: June 9, 2024

✉Address correspondence to jwliu13@ustc.edu.cn

practical applications, including different stimuli (pressure, bending, torsion, and temperature) and extreme conditions, which significantly undermines their precision and selectivity in signal perception, ultimately limiting their working life and application range [25–28]. Therefore, the majority of anisotropic electronic skins can only be applied in the areas of health or motion monitoring, hindering their widespread adoption in other fields.

In spite of the remarkable progress achieved in enhancing the functionalities and performance attributes of anisotropic e-skin, the realization of unimpeded directional strain responses, devoid of the confounding influence of other stimuli, continues to pose a formidable and intricate challenge. Addressing this quandary hinges upon two pivotal factors. One crucial factor is effectively discriminating multidirectional strain signals, which lies in mitigating the occurrence of similar microscopic deformations in e-skin during stretching in any direction [2, 29–34]. Another factor involves sustaining a stable and intact conductive pathway of the e-skin amidst the presence of external interferences through specialized structural design and judicious material selection. Therefore, there is an urgent need to develop anisotropic strain-sensitive e-skin that can effectively resist interference from other stimuli and extreme environments and explore innovative applications.

In this work, a high-performance anisotropic e-skin (HAES) was prepared by a low cost and scalable approach, exhibiting remarkable excellent anti-interference capability. We introduce a unique and special structure of synergistic coexistence of wrinkles of aligned silver nanowires wrinkles and cracks into the HAES. Consequently, the HAES achieves transparency and exhibits excellent anisotropic sensing performance, showing a maximum gauge factor (GF) difference of 2825 and 0.69 for the directions parallel and perpendicular to the alignment of the Ag nanowires (Ag NWs), respectively, which surpasses existing anisotropic e-skins [29, 32, 35–37]. At the same time, the HAES demonstrates ultra-fast response and recover times of 7.5 ms. Moreover, due to the penetration and protection of elastic film on the structure, our e-skin demonstrates superior anti-interference capability even when subjected to high pressure (663 kPa), torsion (540°), bending (180°), temperature variations, and extreme conditions (such as impacts, submersions, and extreme temperatures. This greatly enhances the authenticity of the signals and broadening the operating environment of e-skin. Interestingly, the HAES has been applied in novel applications, including precise undisturbed prediction of crack propagation in terms of size and direction (minimum prediction errors: $|\Delta\varphi|_{min}$ = 3° and $|\Delta\varepsilon|_{min}$ = 0.3%, respectively), as well as manipulation in multimodal soft robotics, leveraging its distinctive features, opening up new avenues for the development of novel e-skin and applications.

2 Experimental

2.1 Device preparation

First, a pre-stretch 80% was applied to the modified polydimethylsiloxane (M-PDMS, the PDMS base:the curing agent:triton = 10:1:0.1 (w/w/w), Sylgard 184, Dow Corning). A grating mask, fabricated by laser cutting, was placed on the upper surface of M-PDMS. Then, Ag NWs (purchased from XF Nano) were sprayed by the airbrush under a pressure of 300 kPa. Finally, the pre-stretched M-PDMS was slowly released and Ag NWs were aligned to realize structure of multiscale stress modulation.

Thermoplastic polyurethane (TPU) gel was prepared via modifying previous method. Simply, 10 ml of N,N-dimethylformamide (DMF) was added in the 4.8 g of TPU grains (Bayer, Desmopan, DP9370A) under adequately stirring for a while. After 24 h, the TPU gel could be obtained. Then, the 1.42 g of TPU gel was dropped on the prepared M-PDMS with structure of multiscale stress modulation and infiltrated in Ag NWs network with the help of capillary force. Thereafter, it was cured at 60 °C for 3 h. Finally, the cured TPU with Ag NWs network was peeled off from M-PDMS, and it was encapsulated with TPU gel by spin coating under a speed of 1000 rpm. The HAES was obtained after curing at 60 °C for 30 min.

2.2 Measurement and characterization

Zeiss Supra 40 equipped with an Oxford PentaFET Precision detector was used to observe scanning electron microscopy (SEM) and energy disperse spectroscopy (EDS). Optical images were collected by Polarizing microscope (OLYMPUS, BX53MTRF-S). Various strains were applied by an Instron 5565A machine. The temperature signals were recorded by data acquisition unit (HIOKI, LR8401-21). The resistance of the MSMA strain sensors were collected by Keithley DMM7510 and 4200 SCS. In addition, the response and recovery times were recorded using the *i*–*t* function of the electrochemical workstation (CHI760D), which features a sufficiently short sampling interval of 0.5 ms, representing less than 1/10 of the response and recovery time. The rebounding process of MSMA strain sensors were captured by high-speed camera (VEO1310L-36G-M).

To analyze the strain distribution and sensing mechanism, finite element analysis (FEA) was conducted by COMSOL Multiphysics. The strain was applied by using Prescribed Displacement (from 0% to 10%) in Solid Mechanics, and the resulting data was analyzed using the First Principal Strain in the results section. Table S1 in the Electronic Supplementary Material (ESM) showed the designed model and the material parameters used for the simulation.

3 Results and discussion

3.1 Structural design of the HAES

The HAES with superior anti-interference capability is fabricated via a simple and scalable nanowire assembly technique (Fig. S1(a) in the ESM). First, Ag NWs with excellent ductility and conductivity are spray-coated onto the pre-stretched substrate with the assistance of a grating mash (Figs. S1(b) and S1(c) in the ESM). It's noteworthy that the modified polydimethylsiloxane (M-PDMS) as a pre-stretched substrate is obtained by mixing Triton X-100 to enhance its stretchability (Fig. S2 in the ESM) [38]. Obviously, the disordered patterned Ag NWs are aligned and stacked into wrinkles perpendicular to the pre-stretched direction upon releasing the substrate, resulting from the shear force [39]. Additionally, cracks also emerge due to Poisson's ratio, which achieves a brilliantly directional response ((i) and (ii) of Fig. 1(a), and Fig. S3 in the ESM). As shown in Fig. S4 in the ESM, the patterned Ag NWs network sprayed on M-PDMS has an ultra-thin grating structure (~ 1.5 μm thick) and exceptional uniformity characterized by the profilometer and confocal microscope.

Subsequently, we choose thermoplastic polyurethane (TPU) to transfer and protect the electrically conductive paths, in which TPU possesses high stretchability and durability (Fig. S5 in the ESM). The Ag NWs networks are fully infiltrated and wrapped after

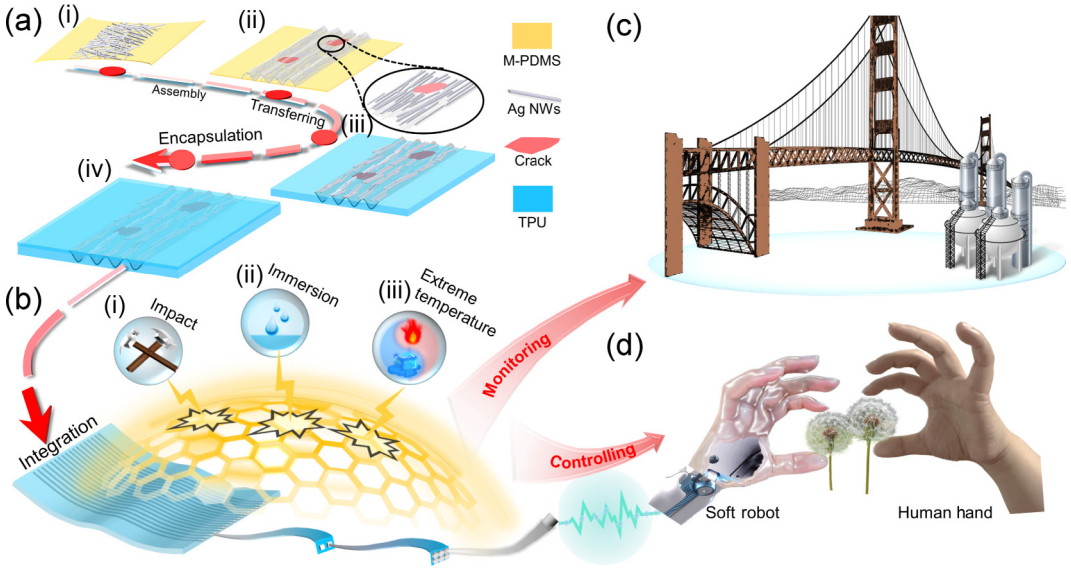

Figure 1 Schematic illustration and applications of anisotropic e-skin. (a) Schematic illustration of microstructure in the preparation process. (b) Schematic illustration of properties of the HAES to resistance (i) impacts, (ii) submersions, and (iii) extreme temperatures. Applications of expansion of (c) cracks monitoring and (d) control of soft robots.

depositing TPU gel due to the aid of the capillary force (Fig. S6 in the ESM). Interestingly, the TPU layer with Ag NW networks (Ag NWs-TPU layer) is easily detached from the M-PDMS, preserving its original structure ((iii) of Fig. 1(a), Figs. S7 and S8 in the ESM). Finally, the anisotropic e-skin is successfully prepared by spin coating another ultra-thin TPU gel (~ 150 μm thick) on the Ag NWs-TPU layer. In this process, the Ag NWs-TPU layer is dissolved once again by the solvent of TPU gel, and then both layers dissolve together to form a seamless integration ((iv) of Fig. 1(a) and Fig. S9 in the ESM). In addition, the e-skin exhibits good transparency, which is an extremely desirable option for skin-mountable devices and an imperceptible integration with the user's skin (Fig. S10 in the ESM). Similar to the muscle fibers protected by elastic connective tissues in Fig. S11 in the ESM, the HAES demonstrates great anti-interference capability to impacts, immersion, and extreme temperature, posing exceptional potential in undisturbed crack propagation monitoring and precise control of soft robots, respectively (Figs. 1(b) and 1(d))

3.2 Sensing performance of the HAES

We conduct a comprehensive analysis of the HAES, including anisotropy, response and recovery time, and minimum detection line. Firstly, to more scientifically and rigorously demonstrate the anisotropy of the device, we adopted a consistent electrode connection method for all tests in this article: the anode and cathode are placed perpendicular to the grating direction (Fig. S12 in the ESM). The tensile strains parallel and perpendicular to the Ag NWs orientation direction are denoted as "0°" and "90°", respectively in Fig. 2(a). Due to the coexistence of the wrinkles and cracks in the aligned Ag NWs, the sensing ability of the sensor exhibits an unbelievable disparity in both directions (Fig. 2(b)). Under tension in the 0° direction, the relative resistance variation $\Delta R/R_0$ is 5.65 × 10^4% at 20% strain. In contrast, $\Delta R/R_0$ is only 13.8% in the 90° direction at the same strain. The GF (the ratio of $\Delta R/R_0$ to strain) in the 0° and 90° direction, corresponds to 2825 and 0.69, respectively at 20% strain. Furthermore, the HAES is connected in series with an light-emitting diode (LED) to modulate its brightness by stretching in different directions to further demonstrate anisotropy (Fig. S13 in the ESM). The HAES also shows great anisotropy and repeatability (Fig. 2(c)). Moreover, Fig. S14(a) in the ESM exhibits that the responses are nearly unaffected by the testing frequencies. Attractively, the HAES is capable of detecting clearly even the subtlest strains, exhibiting an ultralow detection limit of 0.1% strain (Fig. S14(b) in the ESM). In addition, we have added more frequency-related tests (Fig. S15 in the ESM). The experimental results indicate that at low strain, the device performance shows slight variations with frequency. However, as the strain increases, this influence becomes negligible. On the other hand, the response and recovery times are important characteristic in practical application. Our HAES shows a response and recovery time of 7.5 ms at a strain of 1.5% (Fig. 2(d)). Validation of our findings is achieved by capturing the rebounding process using a high-speed camera, which closely matched the recovery times (Fig. 2(e) and Video S1 in the ESM). The durability is another indispensable characterization of the sensor. Figure 2(f) shows that the e-skin remains remarkably stable after 3000 cycles at 5% strain, which indicates that the Ag NW networks wrapped by TPU are sufficiently robust and enduring. In addition, we perform an anisotropic comparison between the HAES and other anisotropic e-skins reported previously, where the HAES possesses the most exceptional performance (Fig. 2(g) and Table S2 in the ESM. GF is defined as $d(\Delta R/R_0)/d\varepsilon$, where ε is strain; GF_1 corresponds to the GF in the most sensitive direction, while GF_2 corresponds to the GF in the least sensitive direction). Furthermore, we vertically integrate two identical devices using substrate-free double-sided adhesive, forming a two-layer composite device (Fig. 2(h)). In this way, when stretched along different directions with various strains (the θ ranges from 0° to 90°, and the strain varies from 0 to 20%), the two devices exhibit distinct responses, enabling the recognition of different stretching directions and strains (Fig. 2(i)).

3.3 Superior anti-interference testing

To prove the anti-interference capability of the HAES, we carry out a systematic exploration. Figures 3(a) and 3(b) display a little signal change of less than 6%, when subjected to pressure (0–663 kPa), torsion (0°–540°), and bending (0°–180°). However, under tension

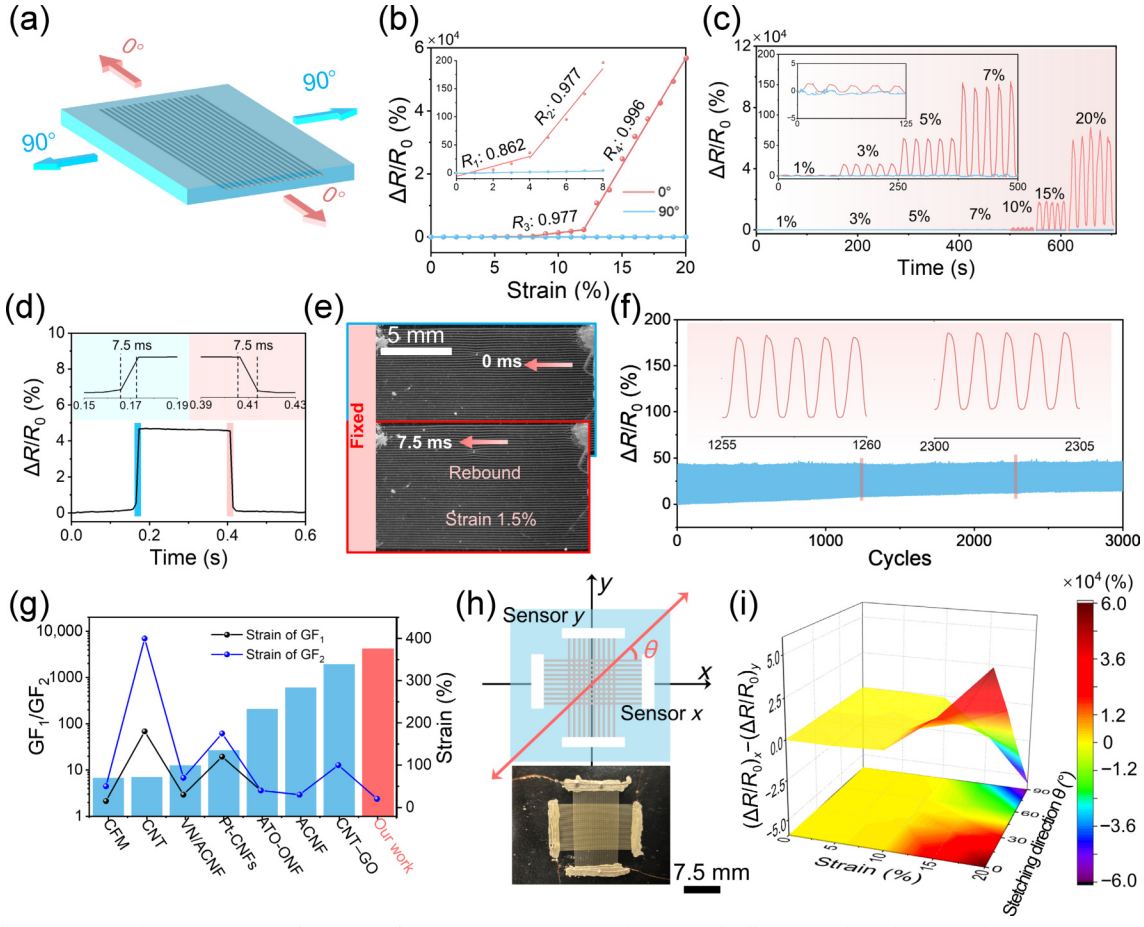

Figure 2 The anisotropy and strain sensing performances of the HAES. (a) Schematic illustration of different stretching directions. (b) The resistance changes of the HAES at directions of "0°" and "90°" in (a), respectively, as a function of strain (red line represents the 0° direction, while the blue line represents the 90° direction). (c) $\Delta R/R_0$ of the HAES at "0°" and "90°" directions at various strains. (d) Response and recovery times of the HAES at 1.5% strain. (e) The high-speed camera photos capturing the rebounding processes of the HAES at 1.5%. (f) Durability and stability of the HAES under the cyclic strain of 5% for 3000 cycles. (g) Comparing the anisotropy of our HAES with previously reported anisotropic strain sensors (the left side represents a bar chart for GF_1/GF_2, while the right side corresponds to the strain curve graph). (h) The equipment diagram (upper) and optical picture (lower) for sensing different directions. Two devices vertically integrated through substrate-free adhesive, referred to as sensor *x* and sensor *y*. θ represents the angle between the applied strain (ε) and the *x*-axis. (i) 3D surface plot of the relationship between applied strain (ε), stretching direction (θ), and $(\Delta R/R_0)_x$–$(\Delta R/R_0)_y$ of the composite device of (h), and the bottom plane is a projection of the 3D profile.

applied along the 0° direction, the $\Delta R/R_0$ is 5.65×10^4% at 20% strain (Fig. 2(b)), which obviously exhibits an excellent selective response for the HAES. It is worth noting that we clamped the sensor at both ends using a mechanical testing machine, and then applied various angles of torsion to the device by rotating the fixture (Fig. S16 in the ESM). The sensor still remains insensitive to bending stimulus after suffering from 60,000 cycles of 180° bending (Fig. S17 in the ESM). To further verify the anti-interference capability of the HAES during stretching, we apply pressures ranging from 0 to 400 kPa when the HAES is stretched to 5% strain in both the 0° and 90° directions (Fig. 3(c)). Interestingly, there is no significant change in the electrical signal even under a pressure of 400 kPa. In contrast, the anisotropy of the sensor is not affected at various pressure (Fig. S18 in the ESM). In addition, the HAES sensor also shows insensitivity to temperature. The $\Delta R/R_0$ only changes from –12.6% to 3.96% when the temperatures are changed from –40 to 80 °C (Fig. S19 in the ESM).

In addition, the anti-interference capability of the HAES to harsh environments is also shown by investigating the sensing performance. As shown in Fig. 3(d), the HAES manifests no response to hammer impacts and maintains its performance unaffected. Additionally, after being repeatedly heated and frozen ten times between 60 and –40 °C, the properties of the HAES do not show any decrease (Fig. 3(e)). It is noteworthy that, due to the larger temperature difference from room temperature (20 °C) to –40 °C ($|\Delta T| = 60$ °C) compared to the temperature difference from room temperature to 60 °C ($|\Delta T| = 40$ °C), and considering that the device is more prone to deformation at low temperatures, the resistance variation at –40 °C is greater than at 60 °C (Fig. S20 in the ESM). Moreover, the sensing performance of the HAES is the same as the initial state when the HAES is soaked in liquid nitrogen (–195 °C) for 28.5 h (Fig. 3(f)). Furthermore, our e-skin not only exhibits a full recovery of its electrical resistance but also shows no evidence of anisotropy damage (Fig. S21 in the ESM). On the other hand, the sensor is capable of withstanding baking at a temperature of 60 °C, and its anisotropy maintains identical in sensing performance (Fig. 3(g)). The HAES demonstrates remarkable stability when used in a variety of liquids, including aqueous and saline solutions (Fig. 3(h)). Figure S22 in the ESM indicates that the contact angle of our device with water is 65.8°. To investigate the long-term stability of the sensor, we immersed it in water. Impressively, the results illustrate that the sensor maintains its stability and cyclic behavior after being submerged in water for a day (Fig. 3(i)), and it retains initial resistance and selective response

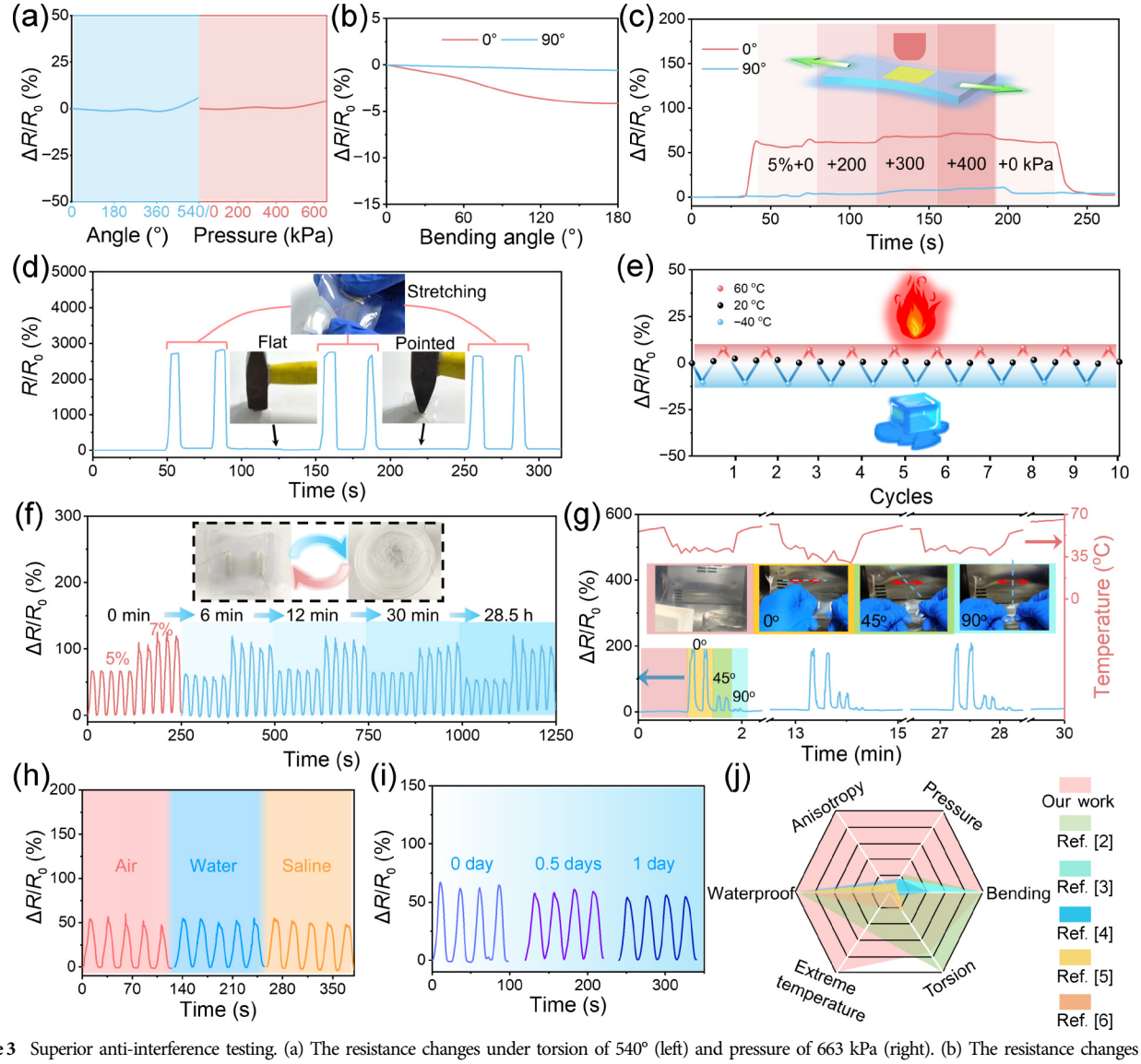

Figure 3 Superior anti-interference testing. (a) The resistance changes under torsion of 540° (left) and pressure of 663 kPa (right). (b) The resistance changes of the HAES to bending in "0°"and "90°" directions. (c) Sensor response to normal pressure for a given initial strain of 5% at "0°"and "90°" directions. (d) the sensing performance resilient to impact of a hammer, including impacts from both the flat end and the pointed end of the hammer. (e) The electrical responses of the sensor under temperature cycles between –40 and 60 °C, showing the stability of structure and insensitivity to temperature. (f) Resistance response of the HAES under 5% and 7% strain after immersion in liquid nitrogen for different durations (up to 28.5 h). (g) Anisotropic sensing performance of the HAES at 0°, 45°, and 90° baked in a 60 °C oven for different durations (red curve represents temperature and blue curve represents the HAES resistance response). (h) The electrical responses of the sensor immersed in air, water, and saline at 5% strain. (i) Long-term stability in water toward 5% strain. (j) Comprehensive performance comparison of the HAES with other strain sensors (the references are listed in Table S2 in the ESM).

even working in water (Figs. S23 and S24 in the ESM). These results suggest that our HAES has an enormous potential to operate in harsh environments on earth due to the anti-interference capability, such as tropical rain forests, deserts, and the North/South Pole regions. Finally, we carry out a comprehensive comparison of the HAES with other previously reported similar type of e-skins, revealing that our e-skin has better performance (Fig. 3(j) and Table S3 in the ESM).

3.4 Anisotropic sensing and resistance mechanisms

A comprehensive analysis has been conducted to elucidate the excellent anisotropy and selective response of the HAES in multi-scenario environments. Firstly, the wrinkles composed of the aligned Ag NWs exist in the grating structure of the HAES (Figs. S8 and S9 in the ESM). The wrinkles are pulled apart and transitioned from a wavy state to a flat state when stretched along perpendicular to the wrinkles, and then return to their initial state after releasing the strain. Furthermore, the aligned Ag NWs demonstrate lateral slippage almost without fracturing, resulting in a negligible change in resistance (Fig. 4(a)). In addition, finite element analysis (FEA) was conducted to simulate strain distribution. The results demonstrate that a small strain exists in the grating and the interconnected Ag NWs when stretched 10% along perpendicular to the grating (Fig. 4(b)), which prevents the internal structure from damage and reduces separation of conductive junctions of Ag NWs. The *in situ* optical microscopy was utilized for real-time observations (Fig 4(c)). It is evident that only wrinkles undergo unfolding and folding without any occurrence of cracks during the stretching and releasing process. This experimental result validates the previous analysis and FEA.

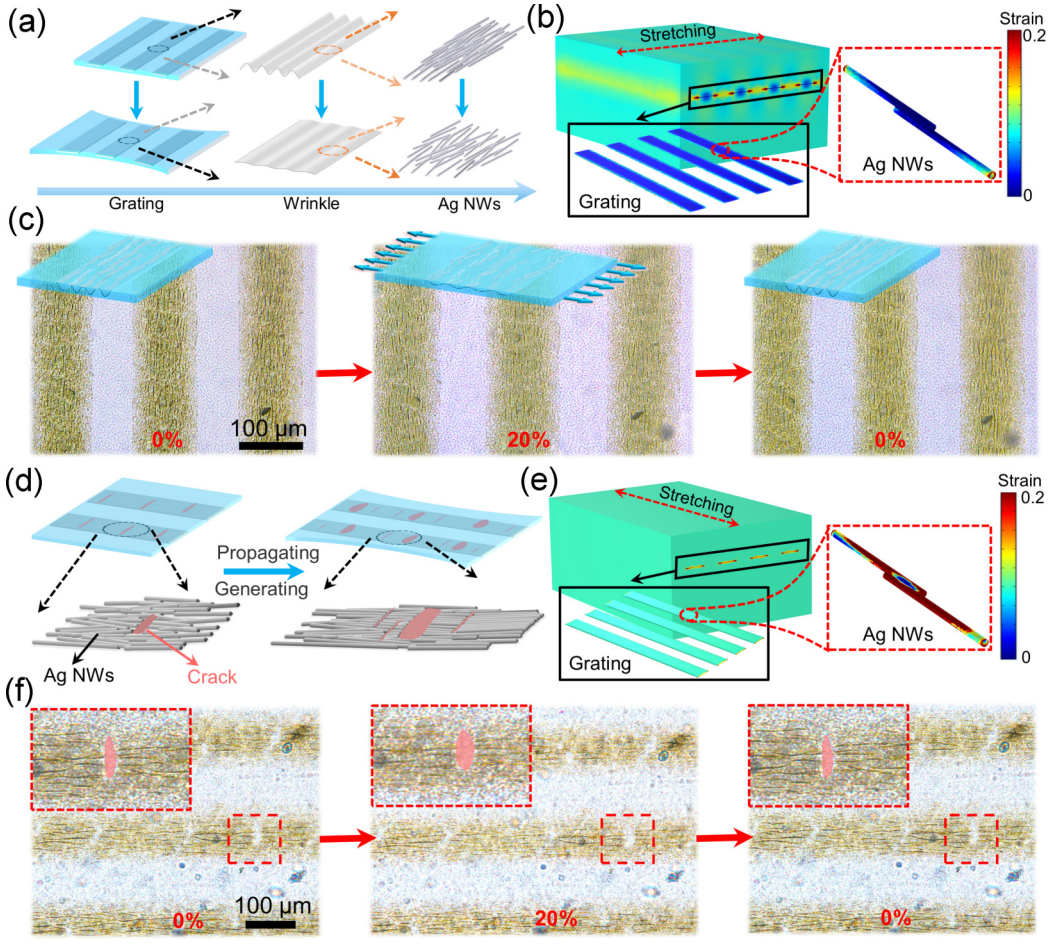

Figure 4 Anisotropic sensing mechanisms of the HAES. (a) Schematic illustration of disperses strain of the wrinkle and aligned Ag NWs. (b) The FEA simulation results of strain distribution of the grating and interconnected Ag NWs when stretched along perpendicular to the grating. (c) *In situ* optical microscopy images of real-time changes of the wrinkle. (d) Schematic illustration of the widening of existing cracks and the formation of new ones under parallel tension. (e) The FEA simulation results of strain distribution of the grating and interconnected Ag NWs under parallel tension. (f) In situ optical microscopy images of real-time changes of cracks.

In contrast, the HAES exhibits a brilliant change in resistance because of the widening of existing cracks and the formation of new ones, caused by the fracturing of Ag NWs under parallel tension (Fig. 4(d)). The FEA results reveal that upon stretched 10% in the parallel direction, the grating undergoes the same deformation of approximately 10% strain, and the strain is concentrated on the interconnected Ag NWs, which shows a significant difference with vertical stretching direction (Figs. 4(b) and 4(e)). Furthermore, the *in situ* optical microscopy was also used to observe real-time broadening and recovery of the cracks (Fig. 4(f)). During this process, the conductive pathways of the Ag NWs experience breakage and reconnection under stretched and released, respectively, which illustrates the significant response of resistance and structural stability. Moreover, minimal strain is distributed around Ag NWs even under conditions of extreme temperature exposure, which ensures the preservation of the sensor's conductivity pathway and selective response (Fig. S25 in the ESM).

3.5 Applications of undisturbed monitoring crack propagation and controlling soft robots.

Due to the unique high sensitivity to various anisotropic strain and anti-interference capabilities of our device, we apply it to undisturbed monitoring of crack expansion size and direction, as well as multi-mode control of soft robots (Figs. 5(a) and 5(b)).

The failure of a structure or material often initiates with the formation of cracks, which may lead to a weakening of material strength, increase the risk of reduced fatigue life, cause stress concentration, result in local deformations, and potentially allow the infiltration of harmful substances. However, due to reasons such as the small size of cracks and the difficulty in determining their propagation direction, it is often challenging to provide early warnings for the expansion of cracks. Consequently, there are significant safety risks for certain structures or containers, such as the collapse of bridges or explosions in high-pressure vessels.

Benefit from the highly sensitive anisotropic features and interference-resistant characteristics of our device, we simulated an application scenario for interference-resistant monitoring of crack expansion size and direction, which holds crucial significance for the advanced prediction and monitoring of damages in critical equipment or structures (Fig. 5(a)). Initially, we vertically integrate two identical devices using substrate-free double-sided adhesive, forming a two-layer composite device (Fig. 2(h)). Consequently, these two devices are then connected to a digital multimeter to collect resistance data (Fig. S26(a) in the ESM). Based on this testing system, we simulated the expansion of cracks using two glass plates and predicted it through the dual-layer composite device (Figs. S26(b) and S27 in the ESM). It is worth noting that monitoring environments in some scenarios are often complex and harsh. For

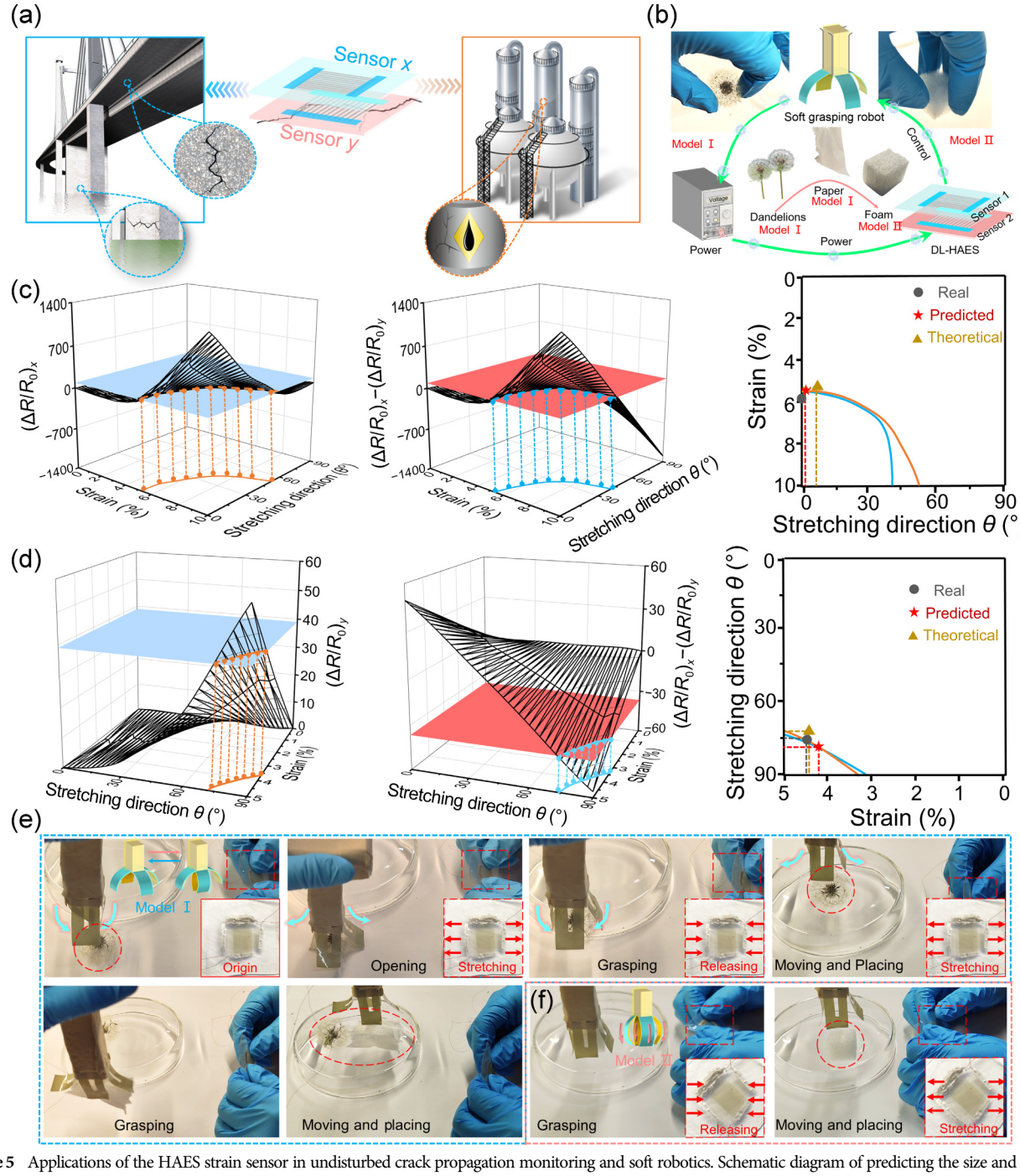

Figure 5 Applications of the HAES strain sensor in undisturbed crack propagation monitoring and soft robotics. Schematic diagram of predicting the size and direction of crack propagation on significant structures or special containers (a) and manipulation of soft robots to imitate human hand (b). (c) and (d) Predicting the size and direction of cracks based on the resistance response of (Fig. S22 in the ESM). The left diagram represents the intersection points of the resistance response (blue plane) for sensor *x* or sensor *y* and the three-dimensional surface plot (black grid lines) of the relationship between applied strain (ε), stretching direction (θ), and $\Delta R/R_0$ of the composite device, along with their projections on the *xy* plane. The middle diagram represents the intersection points of the $(\Delta R/R_0)_x$–$(\Delta R/R_0)_y$ (pink plane) and the three-dimensional surface plot (black grid lines) of the relationship between applied strain (ε), stretching direction (θ), and $(\Delta R/R_0)_x$–$(\Delta R/R_0)_y$ of the composite device, along with their projections on the *xy* plane. The right diagram incorporates the curves of the *xy* plane projections from the left (orange) and middle (blue) diagrams. The black dots represent actual values, while the red pentagrams indicate predicted values. (e) Images of controlling Model I of soft robots to gently and harmlessly grasp and transfer a dandelion and a piece of paper. (f) Images of controlling Model II of soft robots to grasp and transfer a foam cube.

example, bridge monitoring faces challenges such as rain, temperature fluctuations, and even trampling, and monitoring high-pressure vessels is associated with high-pressure environments. These diverse and intricate conditions often have a significant impact on the signals and lifespan of conventional devices. However, in the face of various interferences such as stepping, temperature fluctuations, and water immersion, our device shows no response. When the gap between the two glass plates widens, the device exhibits a resistance response. It is worth noting that the direction of the crack and the strain caused by the crack are

perpendicular, meaning $\theta = (90° - \varphi)$ (θ represents the strain direction, and φ represents the crack direction) (Fig. S28 in the ESM). Furthermore, depending on the size and direction of the crack, the device shows varying responses. Figures 5(c) and 5(d) demonstrate that the predicted points are very close to the actual values and theoretical values. It is noteworthy that the theoretical values are calculated based on the relationship in Fig. 2(b):

$$x_x = \varepsilon \times \cos(90^o - \varphi) \quad (1)$$

$$x_y = \varepsilon \times \sin(90^o - \varphi) \quad (2)$$

$$\Delta R/R_0 = a_1 x + b_1 \;\; 0 \leqslant \Delta R/R_0 < 29.2\% \quad (3)$$

$$\Delta R/R_0 = a_2 x + b_2 \;\; 29.2 \leqslant \Delta R/R_0 < 186.1\% \quad (4)$$

$$\Delta R/R_0 = a_3 x + b_3 \;\; 186.1 \leqslant \Delta R/R_0 < 2314.2\% \quad (5)$$

In these equations, $\Delta R/R_0$ represents the change in resistance, x_x represents strain in the x-axis direction, x_y represents strain in the y-axis direction, ε represents strain caused by cracks, a represents the slope, and b represents the intercept. Based on the resistance response values, the corresponding formula is determined for calculation.

For example, in Fig. 5(d), $(\Delta R/R_0)_y$ and $(\Delta R/R_0)_x$ are 32.9% and 5.2%, respectively. Calculating according to the mentioned formula, the theoretical values are $(90° - \varphi) = 72°$ and $\varepsilon = 4.4\%$. Furthermore, according to the three-dimensional surface plot, the predicted angle of the crack is approximately $(90° - \varphi) = 78°$, and the predicted magnitude of the crack is approximately $\varepsilon = 4.2\%$, which demonstrates an extremely high level of accuracy (the actual angle is $(90° - \varphi) = 75°$, and the actual magnitude is $\varepsilon = 4.5\%$, minimum prediction errors, defined as |actual values–predicted values|: $|\Delta\varphi|_{min} = 3°$ and $|\Delta\varepsilon|_{min} = 0.3\%$ respectively). Furthermore, we have compiled a table summarizing the actual, predicted, and theoretical values of the cracks to present the test results more clearly (Table S4 in the ESM).

Precise control is another significant property of strain sensors to manipulate electronic devices [40–42]. Thus, the HAES was employed to interference-free manipulate double models soft robot similar to the grab of human by utilizing the anisotropy of e-skin (Fig. 5(b) and Fig. S29 in the ESM). Traditional robotic arms controlled by motors often have complex wiring and mechanical structure, and struggle to grasp fragile objects such as dandelions. On the contrary, the soft robot enables addressing these issues resulting from its simple working principle and circuitry. In Fig. 5(b) and Fig. S30 in the ESM, orthogonally stacking double layers of HAESs (DL-HAESs) are performed to control four claws of the soft grasping robot, where the top e-skin (sensor 1) and the bottom e-skin (sensor 2) are connected with claws 1, 3 and claws 2, 4, respectively. In the initial state, the claws of the soft grasping robot are open and then they are folded driven by joule heat after being powered on. Subsequently, the angle of opening and the working models of the soft grasping robot are regulated by stretching the DL-HAESs with different strains and directions, respectively. When stretched along 0° or 90°, due to the anisotropy of the device, only one sensor resistance (sensor 1 or sensor 2) rapidly increases, resulting in a sharp decrease in current in the series circuit, thereby reducing joule heating. Consequently, only one pair of claws (claws 1, 3 or claws 2, 4) is controlled instead of all four claws, in order to minimize damage to the fine structure. This constitutes Model I. The soft robot in Model I gently grasps the light, fragile, and flat objects (dandelion and paper), and transfers them to the designated position (Figs. 5(b) and 5(e)). In addition, when stretched along the 45° direction, the resistance of both sensors (sensor 1 and sensor 2) increases, causing a decrease in current in both series circuits, resulting in reduced joule heating. Therefore, all four claws (claws 1–4) are controlled, constituting Model II. The four claws in Model II are manipulated simultaneously to stably grasp block-shaped objects (foam blocks) and place them to the designated position (Figs. 5(b) and 5(f)). Moreover, Fig. S31 in the ESM exhibits the resistance changes of the DL-HAESs used in Model I and Model II, respectively. In Model I, due to the selective response in different directions and stacked orthogonally of double layers, only one sensor responds when stretched in 0° or 90° directions, which controls the corresponding pair of claws (Fig. S31(a) in the ESM). However, the resistances of the two sensors are changed when stretched in 45° direction, allowing for the manipulation of the two pairs of claws (Fig. S31(b) in the ESM).

4 Conclusion

To summarize, we report a high-performance e-skin with the coexistence of wrinkles and cracks, outstanding anisotropic strain sensing performance, and superior anti-interference capability. The HAES exhibits remarkable anisotropic, ultra-fast response and recover times, and ultralow detection limit due to the coexistence of wrinkles and cracks. In addition, it presents superior anti-interference capability to other stimuli and harsh conditions. Based on these special properties, we utilize the HAESs to undisturbedly predict crack propagation with minimal error that involve multiple stimuli or harsh environments. Finally, by vertically integrating two HAESs, we have enabled precise and interference-free manipulation of the soft robot for grasping objects with different hardness and shapes, including brittle dandelions, flat paper, and sturdy foam blocks in different models. These applications highlight the exceptional capabilities, practicability, and potential of HAES in providing early warnings for the potential destruction of special structures or containers, as well as enhancing advanced robotic systems with improved dexterity and manipulability.

Electronic Supplementary Material: Supplementary material (SEM, EDS, confocal microscope, tensile stress–strain curve, transmittance spectrum measurements, and relevant electrical tests) is available in the online version of this article at https://doi.org/10.26599/NR.2025.94906990.

Data availability

All data needed to support the conclusions in the paper are presented in the manuscript and the Electronic Supplementary Material. Additional data related to this paper may be requested from the corresponding author upon request.

Acknowledgements

This work was supported by the National Natural Science Foundation of China (No. 22175164) and Strategic Priority Research Program of the Chinese Academy of Sciences (No. XDB0450402). This work was partially carried out at the USTC

Center for Micro and Nanoscale Research and Fabrication, also at the Instruments Center for Physical Science, University of Science and Technology of China.

Declaration of competing interest

All the contributing authors report no conflict of interests in this work.

Author contribution statement

X.-L. L and J.-W. L. conceived the idea. J.-W. L. supervised the project. X.-L. L. and C. C. fabricated the HAESs and conducted the anisotropic electric characterization of the HAESs. X.-L. L., Z.-Y. Y., and Y.-C. G. conducted anti-interference testing. Y.-B. Z. and X.-S. M. carried out the FEA. X.-L. L. and W.-Z. W. conducted the application in structural failure prediction. X.-L. L. and X.-F. F. conducted the application in control of soft robot. X.-L. L., C. C., and J.-W. L. wrote and revised the paper. All authors discussed the manuscript during preparation.

Use of AI statement

None.

References

[1] Zhao, Y.; Gao, W. C.; Dai, K.; Wang, S.; Yuan, Z. Q.; Li, J. N.; Zhai, W.; Zheng, G. Q.; Pan, C. F.; Liu, C. T. et al. Bioinspired multifunctional photonic-electronic smart skin for ultrasensitive health monitoring, for visual and self-powered sensing. *Adv. Mater.* **2021**, *33*, 2102332.

[2] Hong, Y.; Wang, B.; Lin, W. K.; Jin, L. H.; Liu, S. Y.; Luo, X. W.; Pan, J.; Wang, W. P.; Yang, Z. B. Highly anisotropic and flexible piezoceramic kirigami for preventing joint disorders. *Sci. Adv.* **2021**, *7*, eabf0795.

[3] Park, B.; Shin, J. H.; Ok, J.; Park, S.; Jung, W.; Jeong, C.; Choy, S.; Jo, Y. J.; Kim, T. I. Cuticular pad-inspired selective frequency damper for nearly dynamic noise-free bioelectronics. *Science* **2022**, *376*, 624–629.

[4] Zhang, Y. F.; Fu, J. J.; Ding, Y. C.; Babar, A. A.; Song, X.; Chen, F.; Yu, X. G.; Zheng, Z. J. Thermal and moisture managing e-textiles enabled by janus hierarchical gradient honeycombs. *Adv. Mater.* **2024**, *36*, 2311633.

[5] Jiang, Z.; Chen, N.; Yi, Z. G.; Zhong, J. W.; Zhang, F. L.; Ji, S. B.; Liao, R.; Wang, Y.; Li, H. C.; Liu, Z. H. et al. A 1.3-micrometre-thick elastic conductor for seamless on-skin and implantable sensors. *Nat. Electron.* **2022**, *5*, 784–793.

[6] Abramson, A.; Chan, C. T.; Khan, Y.; Mermin-Bunnell, A.; Matsuhisa, N.; Fong, R.; Shad, R.; Hiesinger, W.; Mallick, P.; Gambhir, S. S. et al. A flexible electronic strain sensor for the real-time monitoring of tumor regression. *Sci. Adv.* **2022**, *8*, eabn6550.

[7] Liu, Z. Y.; Qi, D. P.; Hu, G. Y.; Wang, H.; Jiang, Y.; Chen, G.; Luo, Y. F.; Loh, X. J.; Liedberg, B.; Chen, X. D. Surface strain redistribution on structured microfibers to enhance sensitivity of fiber-shaped stretchable strain sensors. *Adv. Mater.* **2018**, *30*, 1704229.

[8] Li, L. L.; Zhao, S. F.; Ran, W. H.; Li, Z. X.; Yan, Y. X.; Zhong, B. W.; Lou, Z.; Wang, L. L.; Shen, G. Z. Dual sensing signal decoupling based on tellurium anisotropy for VR interaction and neuro-reflex system application. *Nat. Commun.* **2022**, *13*, 5975.

[9] Liu, Y. M.; Yiu, C. K.; Zhao, Z.; Park, W.; Shi, R.; Huang, X. C.; Zeng, Y. Y.; Wang, K.; Wong, T. H.; Jia, S. X. et al. Soft, miniaturized, wireless olfactory interface for virtual reality. *Nat. Commun.* **2023**, *14*, 2297.

[10] Dong, L. Z.; Ren, M.; Wang, Y. L.; Wang, G. H.; Zhang, S. Q.; Wei, X. L.; He, J. F.; Cui, B.; Zhao, Y. R.; Xu, P. P. et al. Artificial neuromuscular fibers by multilayered coaxial integration with dynamic adaption. *Sci. Adv.* **2022**, *8*, eabq7703.

[11] Wang, M.; Yan, Z.; Wang, T.; Cai, P. Q.; Gao, S. Y.; Zeng, Y.; Wan, C. J.; Wang, H.; Pan, L.; Yu, J. C. et al. Gesture recognition using a bioinspired learning architecture that integrates visual data with somatosensory data from stretchable sensors. *Nat. Electron.* **2020**, *3*, 563–570.

[12] Su, Q.; Zou, Q.; Li, Y.; Chen, Y. Z.; Teng, S. Y.; Kelleher, J. T.; Nith, R.; Cheng, P.; Li, N.; Liu, W. et al. A stretchable and strain-unperturbed pressure sensor for motion interference-free tactile monitoring on skins. *Sci. Adv.* **2021**, *7*, eabi4563.

[13] Luo, Y. S.; Chen, X. L.; Li, X. M.; Tian, H. M.; Li, S.; Wang, L.; He, J.; Yang, Z. B.; Shao, J. Y. Heterogeneous strain distribution based programmable gated microchannel for ultrasensitive and stable strain sensing. *Adv. Mater.* **2023**, *35*, 2207141.

[14] Yang, B.; Xiong, Y.; Ma, K.; Liu, S. R.; Tao, X. M. Recent advances in wearable textile-based triboelectric generator systems for energy harvesting from human motion. *EcoMat* **2020**, *2*, e12054.

[15] Xue, J. T.; Zou, Y.; Deng, Y. L.; Li, Z. Bioinspired sensor system for health care and human-machine interaction. *EcoMat* **2022**, *4*, e12209.

[16] Kang, D.; Pikhitsa, P. V.; Choi, Y. W.; Lee, C.; Shin, S. S.; Piao, L. F.; Park, B.; Suh, K. Y.; Kim, T. I.; Choi, M. Ultrasensitive mechanical crack-based sensor inspired by the spider sensory system. *Nature* **2014**, *516*, 222–226.

[17] Araromi, O. A.; Graule, M. A.; Dorsey, K. L.; Castellanos, S.; Foster, J. R.; Hsu, W. H.; Passy, A. E.; Vlassak, J. J.; Weaver, J. C.; Walsh, C. J. et al. Ultra-sensitive and resilient compliant strain gauges for soft machines. *Nature* **2020**, *587*, 219–224.

[18] Zhang, H.; Chen, H. M.; Lee, J. H.; Kim, E.; Chan, K. Y.; Venkatesan, H.; Shen, X.; Yang, J. L.; Kim, J. K. Mechanochromic optical/electrical skin for ultrasensitive dual-signal sensing. *ACS Nano* **2023**, *17*, 5921–5934.

[19] Li, J. Y.; Li, S.; Su, Y. W. Stretchable strain sensors based on deterministic-contact-resistance braided structures with high performance and capability of continuous production. *Adv. Funct. Mater.* **2022**, *32*, 2208216.

[20] Wang, J. Q.; Wu, B. H.; Wei, P.; Sun, S. T.; Wu, P. Y. Fatigue-free artificial ionic skin toughened by self-healable elastic nanomesh. *Nat. Commun.* **2022**, *13*, 4411.

[21] Hua, Q. L.; Sun, J. L.; Liu, H. T.; Bao, R. R.; Yu, R. M.; Zhai, J. Y.; Pan, C. F.; Wang, Z. L. Skin-inspired highly stretchable and conformable matrix networks for multifunctional sensing. *Nat. Commun.* **2018**, *9*, 244.

[22] Shi, C. Q.; Zou, Z. N.; Lei, Z. P.; Zhu, P. C.; Zhang, W.; Xiao, J. L. Heterogeneous integration of rigid, soft, and liquid materials for self-healable, recyclable, and reconfigurable wearable electronics. *Sci. Adv.* **2020**, *6*, eabd0202.

[23] Zhao, S.; Zhu, R. Electronic skin with multifunction sensors based on thermosensation. *Adv. Mater.* **2017**, *29*, 1606151.

[24] Chen, L. R.; Chang, X. H.; Wang, H.; Chen, J. W.; Zhu, Y. T. Stretchable and transparent multimodal electronic-skin sensors in detecting strain, temperature, and humidity. *Nano Energy* **2022**, *96*, 107077.

[25] Liu, Z. K.; Zheng, Y.; Jin, L.; Chen, K. L.; Zhai, H.; Huang, Q. Y.; Chen, Z. D.; Yi, Y. P. Q.; Umar, M.; Xu, L. L. et al. Highly breathable and stretchable strain sensors with insensitive response to pressure and bending. *Adv. Funct. Mater.* **2021**, *31*, 2007622.

[26] Oh, J.; Yang, J. C.; Kim, J. O.; Park, H.; Kwon, S. Y.; Lee, S.; Sim, J. Y.; Oh, H. W.; Kim, J.; Park, S. Pressure insensitive strain sensor with facile solution-based process for tactile sensing applications. *ACS Nano* **2018**, *12*, 7546–7553.

[27] Wang, H.; Mao, Y. Y.; Ji, D.; Wang, L.; Wang, L.; Chen, J. W.; Chang, X. H.; Zhu, Y. T. Transparent, self-adhesive, highly

environmental stable, and water-resistant ionogel enabled reliable strain/temperature sensors and underwater communicators. *Chem. Eng. J.* **2023**, *471*, 144674.

[28] Chen, J. W.; Wang, F.; Zhu, G. X.; Wang, C. B.; Cui, X. H.; Xi, M.; Chang, X. H.; Zhu, Y. T. Breathable strain/temperature sensor based on fibrous networks of ionogels capable of monitoring human motion, respiration, and proximity. *ACS Appl. Mater. Interfaces* **2021**, *13*, 51567–51577.

[29] Lee, J. H.; Kim, J.; Liu, D.; Guo, F. M.; Shen, X.; Zheng, Q. B.; Jeon, S.; Kim, J. K. Highly aligned, anisotropic carbon nanofiber films for multidirectional strain sensors with exceptional selectivity. *Adv. Funct. Mater.* **2019**, *29*, 1901623.

[30] Zhang, H.; Liu, D.; Lee, J. H.; Chen, H. M.; Kim, E.; Shen, X.; Zheng, Q. B.; Yang, J. L.; Kim, J. K. Anisotropic, wrinkled, and crack-bridging structure for ultrasensitive, highly selective multidirectional strain sensors. *Nano-Micro Lett.* **2021**, *13*, 122.

[31] Chu, Z. M.; Jiao, W. C.; Huang, Y. F.; Zheng, Y. T.; Wang, R. G.; He, X. D. Superhydrophobic gradient wrinkle strain sensor with ultra-high sensitivity and broad strain range for motion monitoring. *J. Mater. Chem. A* **2021**, *9*, 9634–9643.

[32] Jung, D.; Lim, C.; Shim, H. J.; Kim, Y.; Park, C.; Jung, J.; Han, S. I.; Sunwoo, S. H.; Cho, K. W.; Cha, G. D. et al. Highly conductive and elastic nanomembrane for skin electronics. *Science* **2021**, *373*, 1022–1026.

[33] Poloni, E.; Rafsanjani, A.; Place, V.; Ferretti, D.; Studart, A. R. Stretchable soft composites with strain-induced architectured color. *Adv. Mater.* **2022**, *34*, 2104874.

[34] Park, N.; Kim, J. Anisotropic hydrogels with a multiscale hierarchical structure exhibiting high strength and toughness for mimicking tendons. *ACS Appl. Mater. Interfaces* **2022**, *14*, 4479–4489.

[35] Lee, J. H.; Kim, S. H.; Heo, J. S.; Kwak, J. Y.; Park, C. W.; Kim, I.; Lee, M.; Park, H. H.; Kim, Y. H.; Lee, S. J. et al. Heterogeneous structure omnidirectional strain sensor arrays with cognitively learned neural networks. *Adv. Mater.* **2023**, *35*, 2208184.

[36] Chen, S.; Song, Y. J.; Ding, D. Y.; Ling, Z.; Xu, F. Flexible and anisotropic strain sensor based on carbonized crepe paper with aligned cellulose fibers. *Adv. Funct. Mater.* **2018**, *28*, 1802547.

[37] Kim, K. K.; Hong, S.; Cho, H. M.; Lee, J.; Suh, Y. D.; Ham, J.; Ko, S. H. Highly sensitive and stretchable multidimensional strain sensor with prestrained anisotropic metal nanowire percolation networks. *Nano Lett.* **2015**, *15*, 5240–5247.

[38] Kim, J. H.; Kim, S. R.; Kil, H. J.; Kim, Y. C.; Park, J. W. Highly conformable, transparent electrodes for epidermal electronics. *Nano Lett.* **2018**, *18*, 4531–4540.

[39] Zhu, M. G.; Si, J.; Zhang, Z. Y.; Peng, L. M. Aligning solution-derived carbon nanotube film with full surface coverage for high-performance electronics applications. *Adv. Mater.* **2018**, *30*, 1707068.

[40] Wang, H. Y.; Wang, J. Q.; Yao, K. M.; Fu, J. J.; Xia, X.; Zhang, R. R.; Li, J. Y.; Xu, G. Q.; Wang, L. Y.; Yang, J. C. et al. A paradigm shift fully self-powered long-distance wireless sensing solution enabled by discharge-induced displacement current. *Sci. Adv.* **2021**, *7*, eabi6751.

[41] Yan, Y. C.; Hu, Z.; Yang, Z. B.; Yuan, W. Z.; Song, C. Y.; Pan, J.; Shen, Y. J. Soft magnetic skin for super-resolution tactile sensing with force self-decoupling. *Sci. Robot.* **2021**, *6*, eabc8801.

[42] Cai, M.; Jiao, Z. D.; Nie, S. A.; Wang, C. J.; Zou, J.; Song, J. Z. A multifunctional electronic skin based on patterned metal films for tactile sensing with a broad linear response range. *Sci. Adv.* **2021**, *7*, eabl8313.

This is an open access article under the terms of the Creative Commons Attribution 4.0 International License (CC BY 4.0, https://creativecommons.org/licenses/by/4.0/).

© The Author(s) 2025. Published by Tsinghua University Press.